

THE STRUCTURE AND DYNAMICS OF LUMINOUS AND DARK-MATTER IN THE
EARLY-TYPE LENS GALAXY OF 0047-281 AT Z=0.485¹

LÉON V.E. KOOPMANS

California Institute of Technology, TAPIR, 130-33, Pasadena, CA 91125

TOMMASO TREU

California Institute of Technology, Astronomy, 105-24, Pasadena, CA 91125

leon@tapir.caltech.edu, tt@astro.caltech.edu

submitted to *ApJ*

ABSTRACT

We have measured the kinematic profile of the early-type (E/S0) lens galaxy in the system 0047-281 ($z=0.485$) with the *Echelle Spectrograph and Imager* (ESI) on the W.M. Keck-II Telescope, as part of the *Lenses Structure and Dynamics (LSD) Survey*. The central velocity dispersion is $\sigma = 229 \pm 15 \text{ km s}^{-1}$, and the dispersion profile is nearly flat to beyond one effective radius (R_e). No significant streaming motion is found. Surface photometry of the lens galaxy is measured from *Hubble Space Telescope* images. From the offset from the local Fundamental Plane (FP), we measure an evolution of the effective mass-to-light ratio of $\Delta \log M/L_B = -0.37 \pm 0.06$ between $z = 0$ and $z = 0.485$, consistent with the observed evolution of field E/S0 galaxies. (We assume $h_{65} = 1$, $\Omega_m = 0.3$ and $\Omega_\Lambda = 0.7$ throughout.)

Gravitational lens models provide a very accurate mass measurement inside the Einstein radius of $R_E = 8.42 \pm 0.07 \text{ kpc}$. This allows us to break the degeneracy between velocity anisotropy and density profile, typical of dynamical models for E/S0 galaxies. We find that both constant M/L and tangentially anisotropic dispersion models are excluded at $>99.9\%$ CL. The total mass distribution inside R_E can be described by a single power-law density profile, $\rho_t \propto r^{-\gamma'}$, with an effective slope $\gamma' = 1.90^{+0.07}_{-0.20}$ (68% CL; ± 0.1 systematic error). Two-component models yield an upper limit (68% CL) of $\gamma \leq 1.0(1.4)$ on the power-law slope of the dark-matter density profile and a projected dark-matter mass fraction of $0.52(0.42) \pm 0.05$ inside R_E , for Osipkov-Merritt models with anisotropy radius $r_i = R_e(\infty)$. The stellar M_*/L values derived from the FP and dynamical models are found to agree very well.

The results of the LSD survey so far (0047-281 and MG2016+112 at $z=1.004$) indicate that E/S0 galaxies are well described inside their Einstein radii by a constant M_*/L stellar mass distribution embedded in a logarithmic potential, with an isotropic or a mildly radially anisotropic dispersion tensor. These results could indicate that E/S0 galaxies underwent little structural evolution at $z \lesssim 1$ and have a close-to-isothermal total mass distribution in their inner regions. We briefly discuss these results in the context of E/S0 galaxies formation and cold-dark-matter simulations.

Subject headings: gravitational lensing — galaxies: elliptical and lenticular, cD — galaxies: evolution — galaxies: formation — galaxies: structure

1. INTRODUCTION

To understand the evolution and internal structure of luminous and dark matter in early-type galaxies (E/S0), we have started the *Lenses Structure and Dynamics (LSD) Survey*. From an observational point of view, the LSD Survey aims at measuring — using the Keck-II Telescope — the internal (stellar) kinematics of a relatively large sample of E/S0 gravitational-lens galaxies in the redshift range $z = 0 - 1$ (see Treu & Koopmans 2002, hereafter TK02, for a description of the survey and its scientific rationale). The stellar kinematic profiles are combined with constraints from a gravitational-lensing analysis — in particular the mass enclosed by the Einstein radius — in order to break degeneracies inherent to each method individually. In this way, we are uniquely able to constrain the luminous and dark mass distribution and the velocity ellipsoid of the luminous (i.e. stellar) component.

Several of the main questions about E/S0 galaxies that we aim to answer with the LSD Survey are: (i) What is

the amount of dark matter within the inner few effective radii (R_e)? (ii) Does the dark matter density profile agree with the universal profiles inferred from CDM simulations (Navarro, Frenk & White 1997, hereafter NFW; Moore et al. 1998; Ghigna et al. 2001)? (iii) Is there a universal total (luminous plus dark-matter) density distribution that well describes the inner regions of E/S0 galaxies? If so, is it isothermal, as observed in the local Universe and often assumed in lensing analyses? (iv) How does the stellar mass-to-light ratio of E/S0 galaxies evolve with redshift, and does it agree with the evolution of the stellar populations of field early-type galaxies as inferred from Fundamental Plane (hereafter FP) measurements (Treu et al. 1999, 2001a, 2002, hereafter T99, T01a, T02; Kochanek et al. 2000; van Dokkum et al. 2001)? (v) Does the structure of E/S0 galaxies evolve between $z = 0$ and 1 , or is the evolution of the FP purely an evolution of the stellar population? (vi) Is the stellar velocity dispersion tensor isotropic or anisotropic?

¹ Based on observations collected at W. M. Keck Observatory, which is operated jointly by the California Institute of Technology and the University of California, and with the NASA/ESA Hubble Space Telescope, obtained at STScI, which is operated by AURA, under NASA contract NAS5-26555.

First results from the LSD Survey were presented in two recent papers (Koopmans & Treu 2002, hereafter KT02; TK02), where we combined our measurement of the luminosity-weighted stellar velocity dispersion of the lens galaxy in MG2016+112 at $z = 1.004$ with the mass enclosed by the Einstein radius as determined from gravitational lens models (Koopmans et al. 2002). A robust constraint was found on the slope of the total density profile of the lens galaxy, i.e. $\gamma' = 2.0 \pm 0.1 \pm 0.1$ (random/systematic errors) for $\rho_t \propto r^{-\gamma'}$. In addition, we were able to determine the stellar mass-to-light ratio and constrain the slope of the dark-matter halo, leading to a relatively simple self-consistent picture of the lens galaxy: an old and metal-rich stellar component embedded in a logarithmic (i.e. isothermal) potential observed at a look-back time of ~ 8 Gyrs – remarkably similar to many present-day E/S0 galaxies. Constant M/L models were ruled out at a very high confidence level and a significant mass fraction ($\sim 75\%$) of dark matter was shown to be present inside the Einstein radius of about 13.7 kpc. Unfortunately, given the faintness of the galaxy at $z=1$, only a luminosity-weighted velocity dispersion could be obtained and only minimal constraints could be set on the anisotropy of stellar orbits.

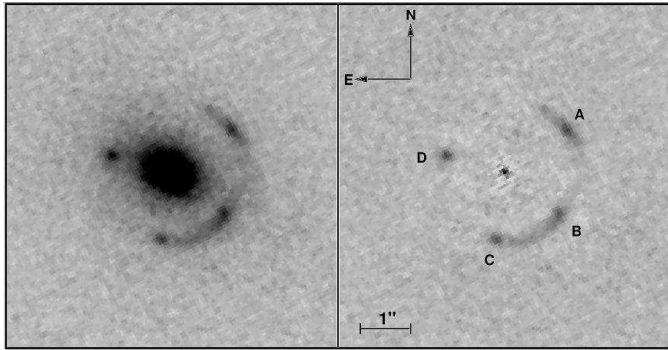


FIG. 1.— Left: HST F555W image of 0047–281. The images are designated A, B, C and D from the upper right going clockwise. Right: Same image with a smooth galaxy model subtracted. Note the almost continuous ring structure including images A, B, and C.

In this paper, we present Keck and HST observations, a gravitational-lens model, and a dynamical model of the lens galaxy in 0047–281 at $z = 0.485$ (Warren et al. 1996, 1998, 1999). This galaxy is bright and sufficiently extended that we were able to measure a spatially resolved velocity dispersion profile, thus setting unprecedented constraints on the orbital structure of a galaxy at a look-back time of ~ 5 Gyrs.

The paper is organized as follows. In Section 2, we describe archival HST observations and spectroscopic observations with ESI on the Keck-II telescope. In Section 3, we analyse these observations and determine the luminosity evolution of the lens galaxy with respect to the local Fundamental Plane. In Section 4, we present a gravitational lens model from which we determine the enclosed mass inside the Einstein radius. In Section 5, we present a model for the luminous and dark-matter distributions of the lens galaxy. In Section 6, the results from the dynamical models are presented. Section 7 summarizes and discusses the results.

In the following, we assume that the Hubble constant,

² Obtained as part of the CASTLeS Survey

the matter density, and the cosmological constant are $H_0 = 65 \text{ km s}^{-1} \text{ Mpc}^{-1}$, $\Omega_m = 0.3$, and $\Omega_\Lambda = 0.7$, respectively. Throughout this paper, r is the radial coordinate in 3-D space, while R is the radial coordinate in 2-D projected space.

2. OBSERVATIONS

2.1. Hubble Space Telescope Imaging

Wide Field and Planetary Camera 2 (WFPC2) images of the system are available from the HST archive, through filters F555W and F814W². In particular, the system has been imaged for 9500s in F555W on the Wide-Field Camera, and 2700s in F814W on the Planetary Camera.

The images were reduced using a series of IRAF scripts based on the IRAF package DRIZZLE (Fruchter & Hook 2002), to align the independent pointings and perform cosmic ray rejection. A subsampled (pixel scale $0''.05$) image was produced for the F555W image. The final “drizzled” image in F555W is shown in Fig.1. Note that for the redshift of the source, $z = 3.595$, Ly- α is redshifted to 5589 Å (Warren et al. 1998) and the F555W magnitude therefore includes the bright Ly- α emission. The F814W image is significantly shallower than the F555W image and although adequate for measuring the structural parameters, it is not particularly useful for the lens modeling, since the multiple images are faint and their positions cannot be accurately determined.

Surface photometry was performed on the F555W and F814W images as described in T99 and Treu et al. (2001b; hereafter T01b). The galaxy brightness profiles are well represented by an $R^{1/4}$ profile, which we fit – taking the HST point spread function into account – to obtain the effective radius (R_e), the effective surface brightness (SB_e), and the total magnitude. The relevant observational quantities of galaxy G in 0047–281 and their errors are listed in Table 1. Note that errors on SB_e and R_e are tightly correlated and that the uncertainty on the combination $\log R_e - 0.32SB_e$ that enters the Fundamental Plane (see Section 3) is very small (~ 0.015 ; see Kelson et al. 2000; T01b; Bertin, Ciotti & del Principe 2002). In the right hand panel of Fig.1 we show the HST image after removal of a smooth model for the lens galaxy. Notice the nearly circular structure of the lensed image configuration around the lens galaxy.

Rest frame photometric quantities listed in Table 1 – computed as described in T01b – are corrected for galactic extinction using $E(B-V)=0.016$ from Schlegel, Finkbeiner & Davis (1998).

2.2. Keck Spectroscopy

We observed 0047–281 using the Echelle Spectrograph and Imager (ESI; Sheinis et al. 2002) on the W.M. Keck-II Telescope during four consecutive nights (23–26 July, 2001), for a total integration time of 20,700s (7x1800s+3x2700s). The seeing was good ($0''.6 < \text{FWHM} < 0''.8$) and three out of four nights were photometric. Between each exposure, we dithered along the slit to allow for a better removal of sky residuals in the red end of the spectrum. The slit (20'' in length) was aligned with the major axis of the galaxy. The slit width of $1''.25$ yields

an instrumental resolution of 30 km s^{-1} which is adequate for measuring the stellar velocity dispersion and removing narrow sky emission lines. The centering of the galaxy in the slit was constantly monitored by means of the ESI viewing camera (the galaxy was bright enough to be visible in a few seconds exposure) and we estimate the centering perpendicular to the slit to be accurate to $\lesssim 0''.1$.

| Redshift (G) | 0.485 ± 0.001 |
|--|-------------------|
| $F814W$ (mag) | 18.67 ± 0.09 |
| $F555W$ (mag) | 20.61 ± 0.09 |
| $\text{SB}_{e,F814W}$ (mag/arcsec 2) | 20.23 ± 0.22 |
| $\text{SB}_{e,F555W}$ (mag/arcsec 2) | 22.59 ± 0.07 |
| $R_{e,F814W}$ (arcsec) | 0.82 ± 0.12 |
| $R_{e,F555W}$ (arcsec) | 0.99 ± 0.04 |
| $b/a = (1 - e)$ | 0.80 ± 0.10 |
| Major axis P.A. ($^\circ$) | 67 ± 5 |
| σ (km s $^{-1}$) | 229 ± 15 |
| M_V (mag) | -22.90 ± 0.04 |
| M_B (mag) | -22.22 ± 0.11 |
| $R_{e,V}$ (kpc) | 5.21 ± 0.72 |
| $R_{e,B}$ (kpc) | 5.82 ± 0.58 |
| $\text{SB}_{e,V}$ (mag/arcsec 2) | 19.29 ± 0.22 |
| $\text{SB}_{e,B}$ (mag/arcsec 2) | 20.39 ± 0.11 |

Table 1.— Observed spectro-photometric quantities of the lens galaxy (G) in Q0047-281. The second part of the table lists rest-frame quantities, derived from the observed quantities as described in Section 2. Note that σ is the central velocity dispersion corrected to a circular aperture of radius $R_e/8$. All quantities in this table assume $H_0 = 65 \text{ km s}^{-1} \text{ Mpc}^{-1}$, $\Omega_m = 0.3$, and $\Omega_\Lambda = 0.7$.

Data reduction was performed using the IRAF package EAS12D³ as described in KT02. To preserve most of the spatially resolved information and to achieve an adequate signal-to-noise ratio at the largest distance for the center of the galaxy, we defined 5 apertures along the spatial direction of the spectrum and summed the signal within each aperture. The apertures correspond approximately to angular dimensions along the slit: $0''.6 \times 1''.25$, $0''.6 \times 1''.25$, $0''.4 \times 1''.25$, $0''.6 \times 1''.25$, $0''.6 \times 1''.25$ (centered respectively at $-1''.1$, $-0''.5$, $0''$, $0''.5$, $1''.1$ along the major axis). A velocity dispersion profile was measured with the Gauss–Hermite Pixel-Fitting Software (van der Marel 1994) and the Gauss Hermite Fourier Fitting Software (van der Marel & Franx 1993) on the spectral region including the G-band ($\sim 4304 \text{ \AA}$), using as kinematic templates spectra of G–K giants observed at twilight with a $0''.3$ slit width, appropriately smoothed to match the instrumental resolution of the $1''.25$ slit. The two codes provide consistent measurements. The total error on velocity dispersion was estimated by adding in quadrature the formal uncertainty given by the codes, the scatter in the results obtained with different templates and the semi-difference of the results obtained with the two codes. The fit to the spectrum from the aperture including part of the brightest lensed images (A and B) was poor, with severe mismatch and unstable measurements. We interpret this as due to contamination by emission from the lensed images. We discarded this measurement from the analysis. The velocity dispersion profile was then folded around the center, as determined

by fitting the centroid of the light distribution at the wavelength of the G band, and the velocity dispersion averaged in the corresponding apertures (symmetric apertures provided results within the errors). The final results are listed in Table 2.

| Aperture (\square'') | σ (km s $^{-1}$) | $\Delta\sigma$ (km s $^{-1}$) |
|---------------------------------|--------------------------|--------------------------------|
| $(0.0\text{--}0.2) \times 1.25$ | 219 | 12 |
| $(0.2\text{--}0.8) \times 1.25$ | 212 | 14 |
| $(0.8\text{--}1.4) \times 1.25$ | 205 | 13 |

Table 2.— Kinematic data along the major axis of 0047–281. The adjacent rectangular apertures are indicated. The seeing was $0''.7$ during the observations.

Using the procedure detailed in T01b, the value in the central aperture can be corrected to standard central velocity dispersion of $\sigma = 229 \pm 15 \text{ km s}^{-1}$ within a circular aperture of radius $R_e/8$ (see also Sec.6.1). No evidence for significant streaming motions (e.g. rotation) was found, with an upper limit of 50 km s^{-1} relative radial velocity between the center and the outermost aperture.

3. THE FUNDAMENTAL PLANE AND THE EVOLUTION OF STELLAR POPULATIONS

Early-type galaxies in the local Universe occupy a two-dimensional manifold in the three-dimensional space defined by the parameters effective radius (R_e), effective surface brightness (SB_e) and central velocity dispersion (σ),

$$\log R_e = \alpha \log \sigma + \beta \text{SB}_e + \gamma_{\text{FP}} \quad (1)$$

known as the Fundamental Plane (hereafter FP; Dressler et al. 1987; Djorgovski & Davis 1987).

In recent years, it has been shown that a similar correlation between those observables exists in clusters out to $z \sim 0.8$ (e.g. van Dokkum & Franx 1996; Kelson et al. 1997; Bender et al. 1998; Pahre 1998; van Dokkum et al. 1998; Jørgensen et al. 1999; Ziegler et al. 2001). The observed evolution of the intercept γ_{FP} of the FP with redshift is consistent with the expectations of passive evolution models for an old stellar population (redshift of formation $z_f \gtrsim 2$; see e.g. van Dokkum et al. 1998). No evidence for a dramatic evolution of the slopes α and β of the FP with redshift is found with the available data (see Jørgensen et al. 1999, Kelson et al. 2000, and T01a for discussion). The correlation is observed to be tight also in intermediate redshift field samples, although a faster evolution of the intercept is found in the highest redshift field samples (to $z \sim 0.7$) and interpreted as evidence for secondary episodes of star formation in the field population at $z < 1$ (T02; see also T99, T01a, Kochanek et al. 2000, van Dokkum et al. 2001, Trager et al. 2000).

Assuming that galaxy G in 0047–281 lies on a FP with slopes similar to those in the local Universe – and pure luminosity evolution – we can determine the offset of its effective mass-to-light ratio ($M/L \propto \sigma^2 10^{-0.4 \text{SB}_e / R_e}$) with respect to the local relation, which is related to the evolution of the intercept by $\Delta \log M/L = -0.4 \Delta \gamma_{\text{FP}} / \beta$. As the local FP in the B band we adopt the relation found by Bender et al. (1998), i.e. $\alpha = 1.25$, $\beta = 0.32$,

³ developed by D. Sand and T. Treu; Sand et al. (2002), in prep.

and $\gamma_{\text{FP}} = -8.895 - \log h_{50}$. In this way, we obtain $\Delta \log M/L_B = -0.37 \pm 0.06$. The error is dominated by the observed FP parameters of galaxy G and dominates uncertainties on the local FP relation. In Fig.2 we plot the evolution of the effective M/L for cluster and field E/S0 galaxies as function of redshift (dashed and solid line; from T02), together with the value obtained for galaxy G (large filled square). The effective M/L evolution for galaxy G is consistent with what is observed for field galaxies, i.e. faster than for the cluster sample, possibly indicating younger luminosity-weighted stellar populations (see, e. g., T01a, T02). As described and discussed in TK02, we can use this measurement to *predict* the stellar mass-to-light ratio (M_*/L_B) of galaxy G assuming that

$$\log(M_*/L_B)_z = \log(M_*/L_B)_0 + \Delta \log(M/L_B), \quad (2)$$

where the second term on the right hand side of the equation is measured from the evolution of the FP, and the first term on the right hand side of the equation can be measured for local E/S0 galaxies. Note that Equation 2 uses the non-trivial assumption that the stellar mass is a redshift-independent function of the combination of observables used to define the effective mass $\sigma^2 R_e$ (for a full discussion see T02, and TK02). Using the local value of $7.3 \pm 2.1 \text{ M}_\odot/\text{L}_{B,\odot}$ determined from data by Gerhard et al. (2001) as in TK02, we predict $M_*/L_B = 3.1 \pm 1.0 \text{ M}_\odot/\text{L}_{B,\odot}$ for galaxy G.

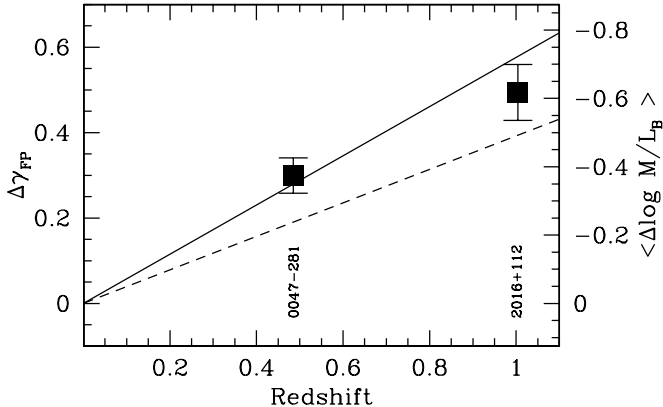


FIG. 2.— Evolution of the M/L as inferred from the evolution of the FP. The solid and dashed lines indicate linear fits to the M/L evolution for field (T02) and cluster E/S0 galaxies (van Dokkum et al. 2001) respectively. The large filled square at $z = 1.004$ indicates the M/L evolution of galaxy D in MG2016+112 (KT02) while the large filled square at $z = 0.485$ represents galaxy G in 0047–281.

4. GRAVITATIONAL-LENS MODEL

The Einstein radius (R_E) and mass enclosed within the Einstein radius, i.e. $M_E \equiv M(< R_E)$ are quantities required in the dynamical models that will be discussed in Sec.5. Both R_E and M_E are very insensitive to the assumed mass profile (see e.g. Kochanek 1991), especially for highly symmetric cases such as 0047–281 (see Fig.1). For simplicity, we model the lens galaxy as a Singular Isothermal Ellipsoid (SIE; Kormann et al. 1994). Although there is an increasing body of evidence favoring this model from lens modeling of individual systems alone (e.g. Chen, Kochanek & Hewitt 1995; Kochanek 1995; Grogan & Narayan 1996; Koopmans & Fassnacht 1999; Cohn et

al. 2001; Muñoz, Kochanek & Keeton 2001; Rusin et al. 2002), we emphasize that the choice of the mass profile does *not* bias the determination of the quantities used in our analysis, i.e. M_E and R_E . Constraints on the mass density profile obtained in Sec.5 are therefore *independent* from this choice.

| Image | Δx (") | Δy (") | $\delta(x, y)$ (mas) |
|-------|----------------|----------------|----------------------|
| G | $\equiv 0.000$ | $\equiv 0.000$ | — |
| A | +1.048 | +0.726 | 10,10 |
| B | +0.896 | -0.802 | 10,10 |
| C | -0.126 | -1.165 | 10,10 |
| D | -1.011 | +0.263 | 10,10 |

Table 3.— Centroid image positions of 0047–281 with respect to the centroid of the primary lens galaxy (G).

The centroids of the four lensed images are used as constraints on the lens model (Table 3), assuming errors of 10 mas, i.e. a fifth of a drizzled pixel size. We do not use the flux ratios, in our analysis since they are not only difficult to measure accurately for extended images, but also change as function of position along the arcs and could be affected by differential dust extinction (e.g. Surpi & Blandford 2002). The position and position angle of the lens-galaxy mass distribution are set equal to those of its surface brightness distribution (Table 1) and the presence of an external shear is allowed for. The velocity dispersion of the SIE mass model is defined such that the enclosed mass within the critical curve is equal to that inside the Einstein radius of a Singular Isothermal Sphere with the same velocity dispersion (Kormann et al. 1994).

4.1. The Isothermal Dark-Matter Velocity Dispersion

The best solution for a single SIE mass distribution has $\chi^2=306$ for 2 degrees of freedom. The velocity dispersion of the primary lens galaxy is found to be $\sigma_{\text{SIE}} = 253 \text{ km s}^{-1}$, whereas the required external shear is 0.13. This single-lens model is clearly not a satisfactory solution.

To improve the model, we add a small companion galaxy with $\rho \propto (1 + (r/r_c)^2)^{-3/2}$ and a slightly softened core ($r_c=0''.01-0''.02$). A range of solutions with $\chi^2 = 0$ is allowed, because the three additional free parameters (position and mass scale) give an underconstrained lens mass model. A lower limit, still yielding a solution with $\chi^2 = 0$, of $\sim 5 \times 10^{-3} M_E$ is found for the mass of this companion galaxy inside a $0''.1$ radius. The distance between the companion galaxy and image D is then $0''.09$ (Fig.3). A Singular Isothermal Sphere (SIS; $\rho \propto r^{-2}$) yields a very similar solution, with a lower limit on its dispersion of $\gtrsim 60 \text{ km s}^{-1}$.

The presence of this companion galaxy lowers the required velocity dispersion of the primary lens galaxy to $\sigma_{\text{SIE}} = 249 \text{ km s}^{-1}$, whereas the external shear becomes 0.07 with a position angle of 173 degrees (north to east). An axial ratio $(b/a)_{\text{SIE}} = 0.63$ is found for the primary lens, broadly in agreement with the ellipticity of the outer surface-brightness isophotes. The random error on σ_{SIE} is well-approximated by $\delta\sigma_{\text{SIE}}/\sigma_{\text{SIE}} = \frac{1}{2}(\delta\theta/\theta_E)$ corresponding to 1 km s^{-1} for our assumed position errors of $\delta\theta \approx 10 \text{ mas}$ (θ_E is the Einstein radius in angular units). Similar results are found from the lens modeling, hence we conclude that the random error on σ_{SIE} is negligible.

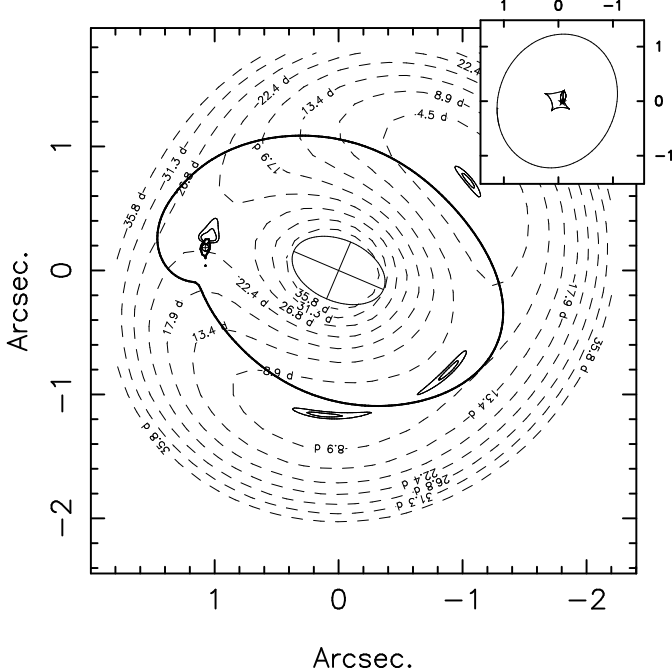


FIG. 3.— Gravitational lens model of 0047-281. The cross-haired ellipse and circle (below image D) indicate the position, position angle and ellipticity of the primary lens galaxy and the companion galaxy, respectively. The thick solid contour is the critical curve, whereas the dashed contours indicate the time-delay surface. To guide the eye, the lensed images are indicated by two contours corresponding to circles in the source plane with 15 and 30-mas radius. The subpanel shows a zoom-in of the caustics. The source position is indicated by a star. Image D is radially extended, perpendicular to the extension of image D apparent in the HST F555W image (see text).

No upper limit can be set on the mass of the companion galaxy, because the lens model is degenerate (see above). There are two reasons, however, why we expect the mass of the companion galaxy not to be much larger than $\sim 5 \times 10^{-3} M_E$. First, no evidence in the HST image (or in the K band image in Warren et al. 1999) is found for a bright companion galaxy close to 0047-281. The nearest galaxy comparable in brightness to G is $\sim 1'$ away (Warren et al. 1999) and contributes at most 0.01 to the local shear and convergence. The luminosity of a companion galaxy must be much less than a percent of that of the primary lens galaxy to go undetected in the HST image. Second, it is found that models with a more massive companion galaxy also require a very large external shear that is perpendicular to the line joining the two galaxies. This indicates that the shear induced by a massive nearby galaxy is exactly compensated for by the external shear. This is a rather contrived situation and there is also no evidence from the HST images that there is any structure in the field that could lead to a very strong external shear.

After the lens modeling, we subtracted a smooth brightness profile from the lens galaxy to search for faint companion galaxies near galaxy G. A faint fuzzy extension to image D at the position, suggested by the lens model, was noticed (see Fig.1). The low S/N ratio of the HST F814W-band image does not allow us to confirm its presence or determine its color. Hence, we can not exclude that this feature is part of the source, even though this extension is tangential to the radially stretched image D. Deeper observations are needed to confirm its presence.

In light of the improved model-fit, the absence of massive nearby galaxies and the agreement between the ellipticities of the light and mass distributions for this model, we will use the mass model with a small companion galaxy near image D as our reference lens model. However, the effect of the companion galaxy on the Einstein mass of galaxy G is small, and taken into account into the error budget as detailed in the next Section.

4.2. The Einstein Radius and Enclosed Mass

Based on our lens model, we adopt the velocity dispersion of $\sigma_{\text{SIE}} = 249 \pm 1 \text{ km s}^{-1}$ for the lens galaxy G. We note that this value is very close to the central stellar velocity dispersion (Table 1). However, we emphasize that σ_{SIE} is a model-dependent expression of the well-determined total enclosed mass, while the central stellar velocity dispersion depends on the precise total mass profile, on the luminous mass profile, and on the dynamical state of the luminous component. Hence, the two quantities do not have to agree in principle. Their agreement is rather an indication of a regular behavior in the physical properties of early-type galaxies, as discussed in Sections 5, 6 and 7 (see also Kochanek 1994 and Kochanek et al. 2000).

The adopted SIE velocity dispersion corresponds to a circular Einstein radius of $R_E = 8.42 \pm 0.07 \text{ kpc}$ (i.e. $\theta_E = 1''.30 \pm 0''.01$) and an enclosed mass of $M_E = 3.81 \times 10^{11} M_\odot$. The errors on R_E and M_E are correlated (both depend on σ_{SIE}): for fixed R_E one finds that $\delta M_E/M_E = 2(\delta\sigma_{\text{SIE}}/\sigma_{\text{SIE}})$. This error corresponds to about 3% for $\delta\sigma = 4 \text{ km s}^{-1}$, i.e. the difference between the model with and without an additional companion galaxy, which we adopt as systematic error (the random error on σ_{SIE} is a negligible 0.5%). By adopting a wide range of mass profiles and/or ellipticities the enclosed mass changes by $\lesssim 4\%$ for symmetric four-image systems like 0047-281 (e.g. Kochanek 1991). Hence, adding the two contributions in quadrature, the total error becomes 5% on M_E inside a radius of $R_E \equiv 8.42 \text{ kpc}$.

5. DYNAMICAL MODEL

5.1. Luminous and Dark-Matter Density Profiles

Following TK02, we model the galaxy mass distribution as a superposition of two spherical components, one for the luminous stellar matter and one for the dark-matter halo. The luminous mass distribution is described by a Hernquist (1990) model

$$\rho_L(r) = \frac{M_* r_*}{2\pi r(r + r_*)^3}, \quad (3)$$

where M_* is the total stellar mass. This profile well reproduces the $R^{1/4}$ surface brightness profile for $r_* = R_e/1.8153$. In Sec.6.1, we also examine the effect of a steeper inner core, $\rho_L(r) \propto r^{-2}$, using the Jaffe (1983) model. We find the effect to be negligible within the errors. The dark-matter distribution is modeled as

$$\rho_d(r) = \frac{\rho_{d,0}}{(r/r_b)^\gamma(1 + (r/r_b)^2)^{(3-\gamma)/2}} \quad (4)$$

which closely describes a NFW profile for $\gamma = 1$, and has the typical asymptotic behavior at large radii found from numerical simulations of dark matter halos $\propto r^{-3}$ (e.g. Ghigna et al. 2000). See TK02 for further discussion of this mass profile and dynamical model.

According to the CDM simulations given in Bullock et al. (2001), a galaxy with the virial mass of galaxy G at $z = 0.485$ has $r_b \approx 50$ kpc $\gg R_e \sim R_E$. Hence, in the light of a comparison with CDM models, we can safely assume that the dark matter profile in the region of interest (i.e. inside $\sim R_E$) is well described by a power-law $\rho_d \propto r^{-\gamma}$. Throughout this study, we will set $r_b = 50$ kpc (effectively equal to $r_b = \infty$). The effects of changing r_b are discussed in TK02.

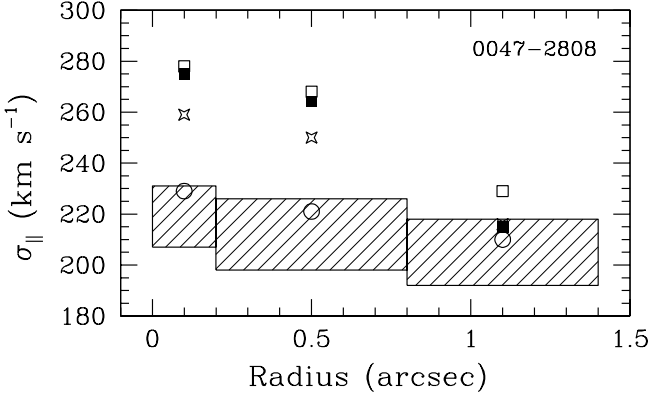


FIG. 4.— Velocity dispersion profile of 0047–281 along the major axis. The box height indicates the 68% measurement error, whereas the box width indicates the spectroscopic aperture (times the slit width 1''.25). The open squares are the corresponding values for an isotropic constant M/L model, whereas the open stars and closed squares are for models with 10% lower M_E (twice its error) and 10% higher R_e (both of which lower σ) with $r_i = \infty$ and $r_i = R_e$, respectively. For reference, the open circles indicate an isotropic Hernquist luminous component embedded in an isothermal total mass distribution, with no adjustments of the model parameters. See Section 6 for details.

In addition, we assume an Osipkov-Merritt (Osipkov 1979; Merritt 1985a,b) parametrization of the anisotropy β of the luminous mass distribution

$$\beta(r) = 1 - \frac{\sigma_\theta^2}{\sigma_r^2} = \frac{r^2}{r^2 + r_i^2}, \quad (5)$$

where σ_θ and σ_r are the tangential and radial component of the velocity dispersion and r_i is called the anisotropy radius. Note that $\beta > 0$ by definition, not allowing tangentially anisotropic models. A brief discussion of tangentially anisotropic models with negative constant values of β is given in Sec. 6.2.

The line-of-sight velocity dispersion is computed, solving the spherical Jeans equation (e.g. Binney & Tremaine 1987). We correct for the average seeing of 0.7'', during the observations, and average the velocity dispersion – weighted by the surface brightness – inside the appropriate rectangular apertures. For completeness, we rescale the apertures (Table 2) by 0.9 and 1.1 in the directions of the major and minor axes, respectively, such that their projection on the axisymmetric model is equivalent to their projection on an elliptical galaxy with an axial ratio of 0.8, even though this has minimal effects on the model velocity dispersions (< 1%), much smaller than the observational errors. The uncertainties on seeing, aperture size, and galaxy centering are taken into account as systematic errors in the following discussion.

6. LUMINOUS AND DARK MATTER IN 0047–281

The unknown parameters of our dynamical model are M_* , γ , r_i and $\rho_{d,0}$ (we note again that $r_* = R_e/1.8153$ and $r_b = 50$ kpc). We can eliminate one of these parameters using M_E , the mass inside the Einstein radius. We choose to eliminate $\rho_{d,0}$. In addition, we transform M_* into the stellar mass-to-light ratio M_*/L_B , fixing the model luminosity exactly to the value $1.2 \times 10^{11} L_{B,\odot}$. Hence, values of M_*/L_B that we derive from the dynamical model, bears an additional uncertainty of 11%, i.e. the observational error on L_B , whereas M_* , which is used in the models does not have this error. We use the average $R_e = 5.52 \pm 0.55$ kpc of the rest-frame V- and B-band values.

For any given set $\{M_*/L_B, \gamma, r_i\}$ the dynamical model is completely determined and the luminosity-weighted velocity dispersions for each of the three apertures (Table 2) can be computed. The likelihood is determined assuming Gaussian error distributions and the confidence contours using the likelihood ratio statistic.

6.1. Power-Law Models

Before studying the luminous and dark-matter profiles individually, we determine the effective slope (γ') of the total (luminous *plus* dark) matter density profile (ρ_t) inside the Einstein radius. We emphasize that an effective slope of γ' does not imply that the density profile follows $\rho_t \propto r^{-\gamma'}$ exactly, but only effectively.

For MG2016+112 (TK02) we measured an effective slope $\gamma' = 2.0 \pm 0.1 \pm 0.1$ (random and systematic errors), assuming $\rho_t \propto r^{-\gamma'}$. Based on the data in Warren et al. (1998) and Kochanek et al. (2000), we found a similar effective slope for 0047–281. However, the errors were relatively large due to a lack of an extended kinematic profile and the large uncertainty on the velocity dispersion given by Warren et al. (1998). With the data presented here we can perform a more accurate measurement, and set constraints on the anisotropy of the velocity ellipsoid.

In Fig. 5(c), we show the likelihood contours of γ' versus the anisotropy radius r_i , based on our extended kinematic profile of 0047–281. Three main conclusions can be drawn: (i) for a spherical isotropic stellar distribution function ($r_i \rightarrow \infty$) $\gamma' = 1.92 \pm 0.05$ (68% CL) (see also Fig. 4); (ii) a lower limit of $r_i/R_e \gtrsim 0.7$ (68% CL) can be set, implying that the velocity distribution function is isotropic in the inner regions of the galaxy; (iii) marginalizing over r_i , one finds $\gamma' = 1.90^{+0.07}_{-0.20}$ (68% CL).

To assess systematic errors on γ' , we varied M_E and R_e by the total uncertainties $\pm 5\%$ and $\pm 10\%$, respectively. The value of γ' , required to fit the data, changes by ± 0.05 and ± 0.03 , respectively. Other potential sources of errors, such as seeing, aperture corrections, aperture offsets, etc., were found to be negligible. We add both contributions and we conservatively round up to a total systematic error of ± 0.1 , to account for all potential minor sources of error.

Although the outer region of galaxy G is well fit by a Hernquist (1990) model, the inner region with $\rho_L(r) \propto r^{-1}$ is less constrained due to the finite resolution of the HST images. We therefore examined power-law models with steeper inner luminosity density profiles, $\rho_L(r) \propto r^{-2}$, using the model from Jaffe (1983). For both $r_i = \infty$ and $r_i = R_e$, we find that the stellar velocity dispersions change by ≤ 6 km s $^{-1}$. In general, Jaffe models give

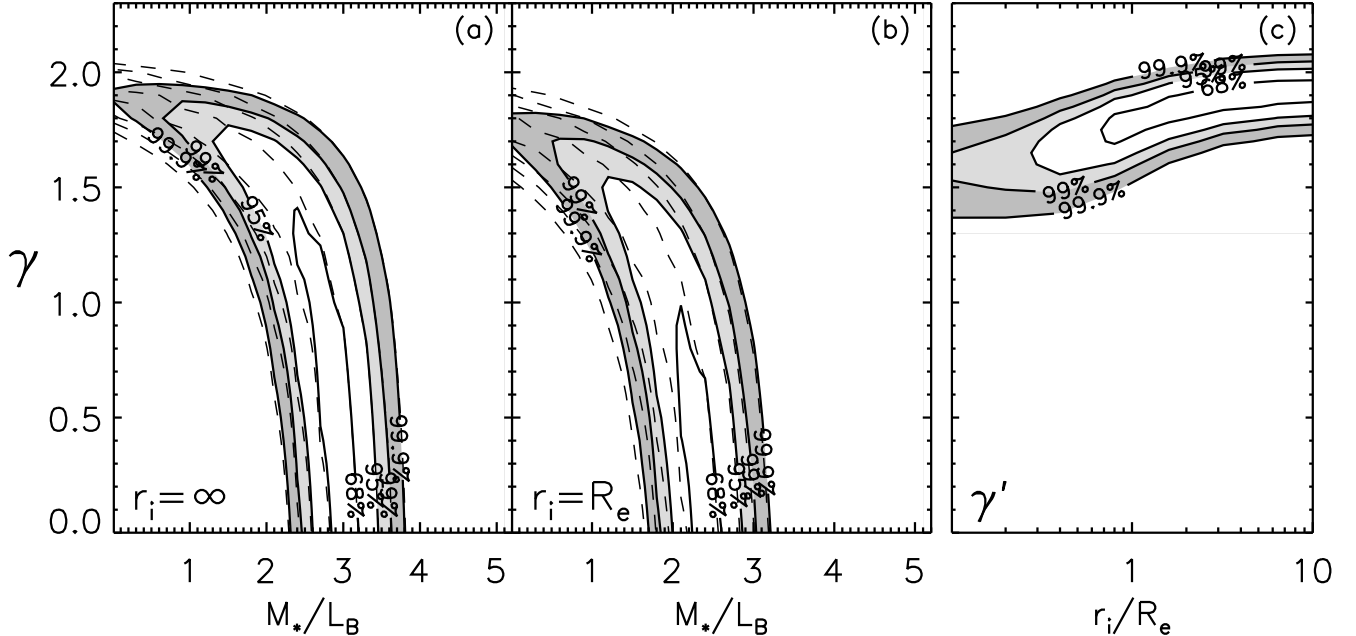


FIG. 5.— Panels (a) and (b) show the likelihood contours of the inner slope of the dark-matter halo (γ) versus the stellar mass-to-light ratio (M_*/L_B) for the lens galaxy in 0047–281, for $r_i = \infty$ and $r_i = R_e$, respectively. The dashed lines indicate the likelihood contours from the dynamical model only, whereas the solid lines combine the constraints from the dynamical model and the FP. Panel (c) shows the likelihood contours of the effective slope (γ') versus the anisotropy radius (r_i). All models assume $r_b = 50$ kpc. See text for a more comprehensive description of the models.

slightly lower velocity dispersions for a fixed value of γ' and the best-fit models therefore yield slightly higher values of γ' (few hundredths) compared with the Hernquist models. However, the differences are not significant, given the errors on dispersion profile, and therefore we conclude that our results are insensitive to the precise shape of the inner luminosity density profile.

For completeness, we note that our model with $\gamma' = 1.90$ results in a central stellar velocity dispersion of $\sigma = 235$ km s $^{-1}$ inside $R_e/8$, in excellent agreement with the empirically derived value of $\sigma = 229 \pm 15$ km s $^{-1}$ in Sec.2.2, confirming the self-consistency of our models.

In conclusion, the total mass distribution of galaxy G is well-matched by a single power-law density profile, that is isothermal (i.e. $\rho_t \propto r^{-2}$) to better than 5%, and the velocity ellipsoid of the luminous component is isotropic at least inside $\sim 70\%$ of the effective radius. Note that this limit is generally consistent with the limits set by other physical considerations. In fact, strongly radial orbits would result in radial instability (e.g. Merritt & Aguilar 1985 find that Osipkov-Merritt models with initial Jaffe density profile are unstable for $r_i \lesssim 0.3r_0$ where $r_0 \approx R_e/0.763$ is the Jaffe half-mass radius; for the effects of a dark matter halo see, e.g., Stiavelli & Sparke 1991) or negative values of the distribution function (e.g. Ciotti 1999, and references therein).

6.2. Constant M/L Models

A stellar mass-to-light ratio of $M_*/L_B = (5.2 \pm 0.8) M_\odot/L_{B,\odot}$ is required to account for the mass M_E , enclosed by the Einstein radius. This is larger than the value $M_*/L_B = (3.0 \pm 1.0) M_\odot/L_{B,\odot}$ derived from the FP

evolution. If we had no kinematic information this could only be interpreted as marginal evidence for dark matter inside the Einstein radius.

However, the velocity dispersion profile changes the situation dramatically: no model where mass follows light can be found to fit the data. For example, in Fig.4 we show the velocity dispersion profile for an isotropic velocity distribution and constant M/L model (open squares). The dispersion falls too sharply with radius and this model can be excluded at the $> 99.9\%$ CL. Even increasing R_e by 10% and decreasing M_E by 10% (twice its error) – both resulting in a smaller stellar velocity dispersion – the fit (open stars) can still be excluded at the $> 99.9\%$ CL. Setting $r_i = R_e$ for the latter model worsens the fit and again the model can be excluded at $> 99.9\%$ CL.

Strong tangentially anisotropic models for lens galaxies (see e.g. Romanowsky & Kochanek 1999), although probably not very likely, can lead to flatter velocity dispersion profiles, even if M/L is constant. We therefore tested models with constant negative values of β . For $\beta \lesssim -1.5$, we find that the dispersion profile indeed becomes flat. However, the predicted stellar velocity dispersion is much higher (i.e. 240–260 km s $^{-1}$) than the observed values and the model is excluded at $> 99.9\%$ CL. Models with $\beta \lesssim -1.5$ can only fit the data when M_E is lowered by $\sim 30\%$. This is at least six times the error on M_E and is incompatible with any acceptable lens model of 0047–281. We therefore conclude that in the lens galaxy G in 0047–281 mass does not follow light, but that M/L increases with radius.

This is a key illustration that knowledge of the enclosed mass, M_E , inferred from the gravitational lens models,

breaks the mass-anisotropy degeneracy.

6.3. Stellar Mass and Dark-Matter Slope

We now turn to the two-component models described in Section 5, to assess the density profile of the halo. In Fig.5 we show the likelihood contours (dashed lines) as a function of the stellar mass-to-light ratio (M_*/L_B) and inner slope of the dark-matter halo (γ). We choose two representative values for the anisotropy radius, $r_i = R_e$ and $r_i = \infty$. We find that: (i) For $M_*/L_B \rightarrow 0$, the slope of the dark-matter halo γ approaches ~ 2 , consistent with the findings of Sec.6.1 (panel c). (ii) For increasing values of M_*/L_B , the total density profile and the velocity dispersion profile become steeper. Hence, γ has to decrease to fit the data.

When we include constraints on M_*/L_B from the Fundamental Plane (Sec.3), the limits tighten on both M_*/L_B and γ (solid contours in Fig.5). Remarkably, we note that the stellar mass-to-light ratio predicted by the FP agrees very well with the range measured from our dynamical models (as for MG2016+112; TK02). In addition, the following limits are found: (i) $M_*/L_B = 3.0^{+0.2}_{-0.6} M_\odot/L_{B,\odot}$ and $\gamma < 1.4$ (68% CL) for $r_i = \infty$ and (ii) $M_*/L_B = 2.4^{+0.2}_{-0.2} M_\odot/L_{B,\odot}$ $\gamma < 1.0$ (68% CL) for $r_i = R_e$. Because the velocity dispersion profile steepens with increasing radial anisotropy, a smaller γ is required to retain a relatively flat dispersion profile. This explains the mild degeneracy between r_i and γ .

In the context of adiabatic contraction (AC) models (e.g. Blumenthal et al. 1986; Mo, Mao and White 1998), the initial slope (γ_i) of the dark-matter halo, i.e. before baryons assembled in the dark-matter potential well, is in general expected to be shallower than the observed DM slope (γ). We find that the difference between γ_i and γ is relatively small, because the stellar mass in the case of 0047–280 is quite extended (i.e. large effective radius) and therefore affects the dark-matter slope less than found in MG2016+112 (TK02), for example. Even in the absence of AC, however, we find that $\gamma_i = 1.5$ (Moore et al. 1998; Ghigna et al. 2001) is inconsistent with the results from 0047–281 at the 95%(68%) CL for $r_i = R_e(\infty)$, whereas the NFW profile ($\gamma_i = 1$; Navarro, Frenk & White 1997) is consistent at the 68% CL for $r_i > R_e$. However, any mechanism, including AC, that steepens the initial slope by more than $\Delta\gamma = \gamma - \gamma_i = 0.4$, would imply that the results from 0047–281 are inconsistent with CDM simulations.

7. SUMMARY & DISCUSSION

We have presented HST and Keck observations of the gravitational lens system 0047-281. In particular, HST images have been used to measure the surface photometry of the lens galaxy G and to build a lensing model of the quadruple-image system. Keck-ESI data have been used to measure a spatially resolved velocity dispersion profile extended beyond the effective radius, with exquisite accuracy ($\sim 5\%$). We have combined all these measurements to study the internal structure and dynamics of the lens galaxy at $z = 0.485$, finding the following:

(i) The offset of galaxy G from the local Fundamental Plane, $\Delta \log M/L_B = -0.37 \pm 0.06$ between $z = 0$ and $z = 0.485$, is consistent with what is observed for field

E/S0 galaxies at similar redshift (T02), i.e. somewhat larger than for cluster E/S0 galaxies. In terms of pure luminosity evolution this could be explained with intermediate age single stellar populations, or – more likely – with secondary episodes of star formation contributing a fraction of young stars to an old underlying stellar population (see discussion in T02).

(ii) Tangential anisotropy of the velocity ellipsoid is excluded at $>99.9\%$ CL. The data are consistent with an isotropic velocity ellipsoid or Osipkov-Merritt (OM) radial anisotropy with anisotropy radius $r_i \geq 0.7R_e$ (68 % CL).

(iii) No dark-matter or constant M/L models are excluded at $> 99.9\%$ CL. The stellar mass-to-light ratio $M_*/L_B = 3.0 \pm 1.0 M_\odot/L_{B,\odot}$ obtained from the offset of the FP is inconsistent with the required $M_*/L_B = 5.2 M_\odot/L_{B,\odot}$ to fully account for M_E . This suggest the presence of dark matter. The FP value is consistent with what is obtained with our two-component dynamical models, and combining the two constraints we find $M_*/L_B = 3.0^{+0.2}_{-0.6} M_\odot/L_{B,\odot}$ (68% CL) for an isotropic velocity ellipsoid. Hence, dark matter comprises a fraction of 0.42 ± 0.05 of the total mass enclosed inside the Einstein radius of 8.4 kpc. Similar results are found for OM anisotropy.

(iv) The total (luminous plus dark) mass distribution inside the Einstein radius is well described by a single power-law density distribution, $\rho_t \propto r^{-\gamma'}$, with $\gamma' = 1.92 \pm 0.05$ (68% CL) for isotropic models, i.e. $r_i = \infty$. In general, $\gamma' = 1.90^{+0.07}_{-0.20}$ (68% CL) is found, marginalizing over r_i . The systematic error is estimated at 0.1.

(v) An upper limit $\gamma \lesssim 1.4$ (68 % CL) is found on the slope on the dark-matter halo inside the Einstein radius for an isotropic model. This limit tightens to $\gamma \lesssim 1.0$ for mildly anisotropic models with $r_i = R_e$. Initial dark-matter profiles with $\gamma_i = 1.5$ (Moore et al. 1998; Ghigna et al. 2001) are therefore marginally excluded, especially since these profile are expected to be less steep before the galaxy assembled. If γ steepens by $\Delta\gamma > 0.4$ during galaxy formation all CDM simulations are inconsistent with our results.

The lens galaxy in 0047–281 appears to convey the picture formulated for MG2016+112 that early-type galaxies at significant look-back times can be effectively described by a $R^{1/4}$ luminous component (modeled in this paper as either a Hernquist or Jaffe profile) embedded in a nearly-isothermal total mass distribution and that their stellar velocity dispersion is relatively isotropic, in particular inside the effective radius. In fact, both lens galaxies in MG2016+112 (KT02, TK02) and 0047–281 show that the total mass distribution is well approximated to within 5% by a simple power law density profile $\rho_t \propto r^{-2}$ (i.e. isothermal).

Even more so, we have shown that deviations from isothermality or isotropy in the lens galaxies of 0047–281 and MG2016+112 quickly lead to inconsistencies with constraints from either the FP, the observed stellar kinematics, the stellar mass-to-light ratio, observations of local E/S0 galaxies, the gravitational-lens models, etc., whereas the models that fit all constraints are internally consistent, appear to agree with all observational constraints available, and indicate both isothermality and near-isotropy.

Constant M/L or steep mass profiles inside the Einstein radius are excluded at very high confidence levels.

A physical explanation is required if isotropy and the almost perfect isothermality are confirmed to be generic features of early-type galaxies (as for late-type galaxies). In particular, this regularity might suggest that luminous and dark-matter were strongly coupled at some point during galaxy assembly. Whereas adiabatic contraction has been suggested as a mechanism that can lead to near-isothermal mass profiles (e.g. Keeton 2001), it is not clear why such a process should only stop when the density profile is isothermal to better than apparently a few percent (see also TK02). Adiabatic contraction also leads to a slope of the inner density profile, inconsistent with the observed absence of lensed images in the centers of lens galaxies (e.g. Keeton 2001), if either the central black holes are not very massive or the inner density profiles do not steepen through some other process. Violent relaxation could be a natural and viable explanation for this regularity, although it should also be explained why luminous and dark matter have *different* density profiles (see discussion in TK02 and references therein). A combination of the two processes during some period in the formation of the galaxy can not be excluded.

The striking similarity of the internal structure of E/S0 galaxies at large look-back times with the internal structure of local E/S0 galaxies (e.g. Franx et al. 1994; Bertin et al. 1994; Rix et al. 1994; Gerhard et al. 2001; see also Kochanek 1995 and reviews by de Zeeuw & Franx 1991; Bertin & Stiavelli 1993; Merritt 1999) suggests that little structural evolution occurred during the past 8 Gyrs (although a larger sample is needed to make a quantitative and general statement). The lack of significant structural evolution is also suggested by the remarkable agreement between the stellar M_*/L_B obtained with our dynamical models and the stellar M_*/L_B estimated using the FP evolution. This fact adds further evidence in favor of a scenario where the general population of massive (field) E/S0 galaxies changed little in the past 8 Gyrs (from $z \sim 1$) –

as indicated for example by the modest evolution in their number density (Schade et al. 1999; Im et al. 2002; Cohen 2002; McCarthy et al. 2002) and by the little evolution in the scatter of the FP (T02) – with most of the evolution being driven by ageing of old stars and secondary episodes of star formation (Jimenez et al. 1999; Trager et al. 2000; Menanteau, Abraham & Ellis 2002; T02).

Finally, we note that the results from the LSD Survey thus far strongly support the often implicit choice for the isothermal mass distribution in the determination of the Hubble Constant (H_0) from time-delays measured from lens systems without apparent massive nearby groups or clusters (e.g. Koopmans & Fassnacht 1999; Koopmans 2001; Kochanek 2002) and calculations of the statistics from well-understood radio-lens surveys, such as the Jodrell-Bank VLA Astrometric Survey (JVAS) and the Cosmic Lens All-Sky Survey (CLASS; see Helbig et al. 1999 and references therein; Falco, Kochanek & Munoz 1998).

We thank Eric Agol, Andrew Benson, Giuseppe Bertin, Roger Blandford, Richard Ellis, Chris Kochanek, and Massimo Stiavelli for useful comments on this manuscript and stimulating conversations. The use of the Gauss-Hermite Pixel Fitting Software and Gauss-Hermite Fourier Fitting Software developed by R. P. van der Marel and M. Franx is gratefully acknowledged. The ESI data were reduced using software developed in collaboration with D. Sand. We acknowledge the use of the HST data collected by the CASTLES collaboration. LVEK and TT acknowledge support by grants from NSF and NASA (AST-9900866; STScI-GO 06543.03-95A; STScI-AR-09222). We thank J. Miller, M. Bolte, R. Guhathakurta, D. Zaritsky and all the people who worked to make ESI such a nice instrument. Finally, the authors wish to recognize and acknowledge the very significant cultural role and reverence that the summit of Mauna Kea has always had within the indigenous Hawaiian community. We are most fortunate to have the opportunity to conduct observations from this mountain.

REFERENCES

Bender R., Saglia R. P., Ziegler B., Belloni P., Greggio L., Hopp U., Bruzual G., 1998, ApJ, 493, 529

Bertin, G., Ciotti, L., del Principe, M., 2002, A&A, 386, 149

Bertin, G., & Stiavelli, M., 1993, Rep. Prog. Phys, 56, 493

Bertin, G. et al. 1994, A&A, 292, 381

Binney, J. & Tremaine, S., 1987, Galactic Dynamics, Princeton University Press, Princeton

Blumenthal, G. R., Faber, S. M., Flores, R., Primack, J. R.

Bullock, J. S., Kolatt T. S., Sigad, Y., Somerville, R. S., Kravtsov, A. V., Klypin, A. A., Primack, J. R., & Dekel, A., 2001, MNRAS, 321, 598

Chen, G. H., Kochanek, C. S., & Hewitt, J. N. 1995, ApJ, 447, 62

Ciotti, L., 1999, ApJ, 520, 574

Cohen, J. G. 2002, ApJ, 567, 672

Cohn, J. D., Kochanek, C. S., McLeod, B. A., & Keeton, C. R. 2001, ApJ, 554, 1216

de Zeeuw, T., & Franx, M., 1991, ARA&A, 29, 239

Djorgovski S. G., Davis M., 1987, ApJ, 313, 59

Dressler, A., Lynden-Bell, D., Burstein, D., Davies, R. L., Faber, S. M., Terlevich, R., Wegner G. 1987, ApJ, 313, 42

Falco, E. E., Kochanek, C. S., & Munoz, J. A. 1998, ApJ, 494, 47

Franx, M., van Gorkom J. H., & de Zeeuw, P.T. 1994, ApJ, 436, 642

Fruchter, A. S. & Hook R. N., 2002, PASP, 114, 144

Gerhard, O., Kronawitter, A., Saglia, R. P., & Bender, R., 2001, AJ, 121, 1936

Ghigna, S., Moore, B., Governato, F., Lake, G., Quinn, T., Stadel, J., 2000, ApJ, 544, 616

Grogan, N. A. & Narayan, R. 1996, ApJ, 464, 92

Helbig, P., Marlow, D., Quast, R., Wilkinson, P. N., Browne, I. W. A., & Koopmans, L. V. E. 1999, A&AS, 136, 297

Hernquist, L., 1990, ApJ, 356, 359

Im, M., Faber, S. M., Koo, D. C., Phillips, A. C., Schiavon, R. P., Simard, L. & Willmer, C. N. A., 2002, ApJ, in press

Jaffe, W. 1983, MNRAS, 202, 995

Jimenez, R., Friaca, A., Dunlop, J. S., Terlevich, R.J., Peacock J. A., Nolan, L. A., 1999, MNRAS, 305, L16

Jørgensen I., Franx M., Hjorth J., van Dokkum P. G., 1999, MNRAS, 308, 833

Keeton, C. R. 2001, ApJ, 561, 46

Kelson D. D., van Dokkum P. G., Franx M., Illingworth G. D., Fabricant D., 1997, ApJ, 478, L13

Kelson D. D., Illingworth G. D., van Dokkum P. G., Franx M., 2000a, ApJ, 531, 137

Kochanek, C. S., 1991, ApJ, 371, 289

Kochanek, C. S., 1994, ApJ, 436, 56

Kochanek, C. S., 1995, ApJ, 445, 559

Kochanek, C. S. et al. 2000, ApJ, 543, 131

Kochanek, C. S., 2002, ApJ, submitted, astro-ph/0204043

Koopmans, L. V. E., 2001, PASA, 18, 179

Koopmans, L. V. E. & Fassnacht, C. D., 1999, ApJ, 527, 513

Koopmans, L. V. E. & Treu, T., 2002, ApJ, 568, L5 (KT02)

Koopmans, L. V. E., Garrett, M. A., Blandford, R. D., Lawrence, C. R., Patnaik, A. R., Porcas, R. W., 2001, MNRAS, in press (K02)

Kormann, R., Schneider, P., Bartelmann, M., 1994, A&A, 284, 285

McCarthy, P. J. et al. 2002, ApJ, 560, L131

Menanteau, F., Abraham, R. G., Ellis, R. S. 2001, MNRAS, 322, 1

Merritt, D. 1985a, AJ, 90, 1027

Merritt, D. 1985b, MNRAS, 214, 25

Merritt, D., 1999, PASP, 111, 129

Merritt, D. & Aguilar, L. A. 1985, MNRAS, 217, 787

Moore, B., Governato, F., Quinn, T., Stadel, J. & Lake, G., 1998, ApJ, 499, L5

Muñoz, J. A., Kochanek, C. S., & Keeton, C. R. 2001, ApJ, 558, 657

Navarro, J., Frenk, C. S., & White S. D. M, 1997, ApJ, 490, 493 [NFW]

Osipkov L. P., 1979, Pis'ma Astron. Zh., 5, 77

Pahre, M. 1998, PhD Thesis, California Institute of Technology

Romanowsky, A. J. & Kochanek, C. S., 1999, ApJ, 516, 18

Rix, H. W., de Zeeuw, P. T., Cretton, N., van der Marel, R. P., & Carollo, C. M. 1997, ApJ, 488, 702

Rusin, D., Norbury, M., Biggs, A. D., Marlow, D. R., Jackson, N. J., Browne, I. W. A., Wilkinson, P. N., & Myers, S. T. 2002, MNRAS, 330, 205

Schade D. et al., 1999, ApJ, 525, 31

Sheinis, A. I., Bolte, M., Epps, H. W., Kibrick, R. I., Miller, J. S., Radovan, M. V., Bigelow, B.C. & Sutin, B.M. 2002, PASP, in press, astro-ph/0204297

Schlegel, D. J., Finkbeiner D. P., Davis M., 1998, ApJ, 500, 525

Stiavelli, M., & Sparke, L., 1991, ApJ, 382, 466

Surpi, G., & Blandford, R. D., 2002, MNRAS, submitted, astro-ph/0111160

Trager S. C., Faber S. M., Worthey G., Gonzalez J. J., 2000a, AJ, 119, 1645

Treu, T. & Koopmans, L. V. E. 2002, ApJ, 575, in press [TK02]

Treu, T., Stiavelli, M., Bertin G., Casertano, C., & Møller, P. 2001a, MNRAS, 326, 237 (T01a)

Treu, T., Stiavelli, M., Casertano, C., Møller, P., & Bertin G. 1999, MNRAS, 308, 1307 (T99)

Treu, T., Stiavelli, M., Casertano, C., Møller, P., & Bertin, G. 2002, ApJ, 564, L13 (T02)

Treu, T., Stiavelli, M., Møller, P., Casertano, C., & Bertin G. 2001b, MNRAS, 326, 221 (T01b)

van der Marel, R. P. 1994, MNRAS, 270, 271

van der Marel R. P., Franx M., 1993, ApJ, 407, 525

van Dokkum P., Franx M., 1996, MNRAS, 281, 985

van Dokkum, P. G., Franx, M., Kelson D. D. & Illingworth G. D., 1998, ApJ, 504, L17

van Dokkum, P. G., Franx, M., Kelson D. D. & Illingworth G. D., 2001, ApJ, 553, L39

Warren, S. J., Hewett, P. C., Lewis, G. F., Møller, P., Iovino, A., Shaver P. A., 1996, MNRAS, 278, 139

Warren, S. J., Iovino, A., Hewett, P. C., Shaver P. A., 1998, MNRAS, 299, 1215

Warren, S. J., Lewis, G. F., Hewett, P. C., Møller, P., Shaver P. A., & Iovino, A. 1999, A&A, 343, L35

Ziegler, B. L., Bower, R. G., Smail, I. R., Davies, R. L. & Lee, D. 2001, MNRAS, 325, 1571